New directions in time-resolved neutron diffraction; Probing high power microwave materials synthesis in situ.

ILL Long Term Proposal (LTP-5A-5).

Final Report

Overview of the project.

This LTP proposed the design and the optimization of an experimental set-up capable of performing *in situ* powder neutron diffraction (PND) of microwave (MW) promoted reactions of ceramic materials (primarily focusing on the synthesis of titanium carbide (TiC), extending then the strategy to other binary and ternary transition metal carbides - group IV, V and VI). The use of MWs for this kind of synthesis has been observed to successfully reduce the reaction time of several orders of magnitude if compared with traditional routes (i.e., conventional furnace), thus being very promising in the field of industrial processing of materials for their fast and green approach [1-9]. However, until now, limitations of in situ measurements techniques have meant that it has been difficult to reproduce results and not easy to understand the mechanism of activation [10].

The first three phases of this project aimed to design and develop the MW set-up and its applicator for processing TiC (milestone one); finding an accurate method for temperature measurements during its synthesis (milestone two), and optimizing the control of all the crucial MW parameters via PC i.e., forward and reflected power and frequency of the MW radiation (milestone three). The last phase (milestone four) has been devoted to expand the method to other d-block binary and ternary carbides, in particular to Nb_2O_5+C and Ta_2O_5+C binary systems and $Ti_{1-x}W_xC_y$, $Ta_{1-x}Ti_xC_y$,$Ti_{1-x}(WO_2)_xC_y$, $Ti_{1-x}(TiO_2)_xC_y$, $Ti_{1-x}(Nb_2O_5)_xC_y$ (with y~1) and $Ti_{1-x}(Ta_2O_5)_xC_y$ (with y~2) ternary systems.

The MW system is now fully operational on D20, which has the capability to follow ultrafast reactions over second timescales, thus giving insight in the synthesis mechanism of MW-promoted processes.

Scientific results.

Phase one was devoted to find the best working conditions of the MW set-up, namely a geometry which can allow the maximum energy transfer into the sample.

This phase followed a “Phase zero”, during which the project, the design and the realization of the applicator (Figure 1) was achieved. This step had to take into account different parameters:

1) D20 beam line - plus MW set-up - geometry constraints;

2) Avoiding possible interactions of the applicator with: neutron beam, MWs, sample.

In our case, commercially available applicators suitable for MW-induced reactions showed three major problems, which lead us to choose an *ad hoc* design: 1) they are not implemented for D20 beam line, which has precise geometry constraints; 2) their materials could give problems in terms of neutron activation; 3) their shape, mostly rectangular, could have lead to very complex diffraction patterns.

We decided then to build the applicator in aluminum (4mm thickness), which is a good compromise in terms of costs and problems of neutron activation (answering to both point 1 and 2). Plus, 1 mm of Al gives an attenuation of neutron beam intensity of 1%, which we found reasonable for our purposes.

Point 3 has been overcome by using a cylindrical shape, which avoids further complications in data reduction.

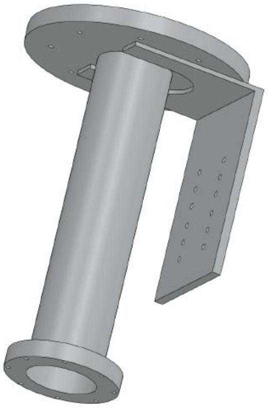

Fig. 1. Final shape of the applicator. It responds to multiple problems, such as avoiding interference with both the sample and the neutron beam, fitting D20 geometry constraints and avoiding activation risks.

On the other side, a cylindrical shape represents an uncommon choice for MW applicators; for this purpose, simulations of the electromagnetic field in such a cavity have been performed (Figure 2). Figure 2a shows a 3D snapshot of the portion of the system that comes after the MW generator, isolator and tuner (see Figure 3 for details). Only the inner dimensions of the system are shown, because essentially the fields don't penetrate the walls of the waveguide, so there is no need to model their thickness (and similarly, we accounted for flanges but they are not explicitly shown).

The power enters from the left hand side (the rectangular section), goes round the bend and then down the tube. A choke is also included (black arrow) for pyrometer readings; however we decided to exclude it in the final design, as we chose another system for temperature measurements (see Phase two for details).

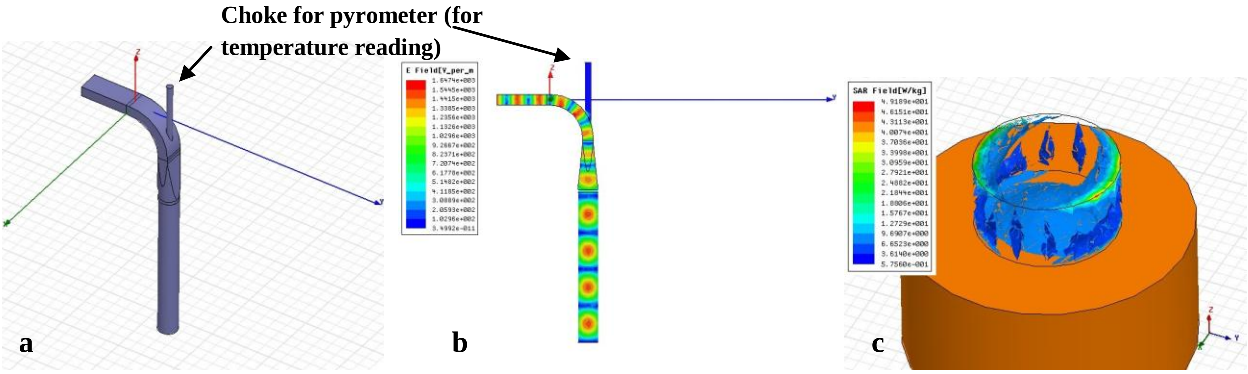

Fig.2 a) 3D image of the applicator (and bend waveguide). In a) and b), a choke for pyrometer is visible (black arrow). The choke has been taken into account in the simulations, but then eliminated in the final design; b) Plot of the electric field magnitude; c) sample heating simulation (the cylindrical orange part is the sample holder, here in boron nitride).

A standing wave is formed in the applicator - because it is terminated with a short circuit, i.e., a metallic plate which closes the applicator at the bottom. The first electric field maximum is found ~72mm off the short which is a quarter of the wavelength, (λ=281mm, when running at 2.45GHz frequency). Being a standing wave, other maxima will be periodically found in the applicator (red spots in Figure 2b).

These simulations gave us a starting point for our experiments: in fact, the position of the maxima changes when a sample is placed into the applicator, because its dielectric properties perturb the electromagnetic field. Consequently, once placed our pellet at around 70mm from the short – as the simulation suggests - all the parameters were tuned and optimised, until the best working conditions were satisfactorily achieved (maximum forward power - and hence maximum heating - transferred into the sample).

This applicator permits now to perform in situ MW-promoted high temperature-high speed reactions, avoiding any possible interference with sample, MWs and neutron beam.

Our single mode MW set-up is composed of: a Sairem GMP20K MW generator (Figure 3(1)), with a 2.45GHz frequency-2KW power magnetron; an isolator (Figure 3(2)) – which prevents the reflected power (i.e., the power not absorbed by the sample) to go downstream the magnetron, avoiding damages; a quartz window (Figure 3(3)) – which prevents damages to the magnetron in case of an arc[1]; a manual variable 3-stub tuner (Figure 3(4)) - which allows to resize the cavity to make it resonant at the 2.45GHz frequency of the source, as the presence of the sample perturbs the resonant frequency; a cylindrical

---

[1] An electric arc is an electrical breakdown of a gas that produces a plasma discharge. It causes a current through a normally non-conductive medium (for example, air).

applicator (Figure 3(6)), as described above and the power supply (Figure 3(7)). Further, a MW survey meter (Figure 3(8)) warns the operator in case of a MW leakage.

All these bits are connected through the most common and commercially available waveguide type WR340, with inner dimensions of 86x43 mm, except for the applicator - which has an 80 mm inner diameter and therefore required a rectangular-to-cylindrical transition waveguide (Figure 3(5)).

We experienced an arc during 21st-23rd May beam time: the quartz window was not yet in place and the formation of a plasma inside the cavity caused an electric discharge going downstream to the isolator: the ferrites –magnets placed inside the isolator for diverging the reflected power, avoiding it to go back to the generator – have been completely destroyed by the arc.

Different geometries of the MW set-up have been tested (see below, Figures 7(a) and (b)), before finding the working one (Figure 3).

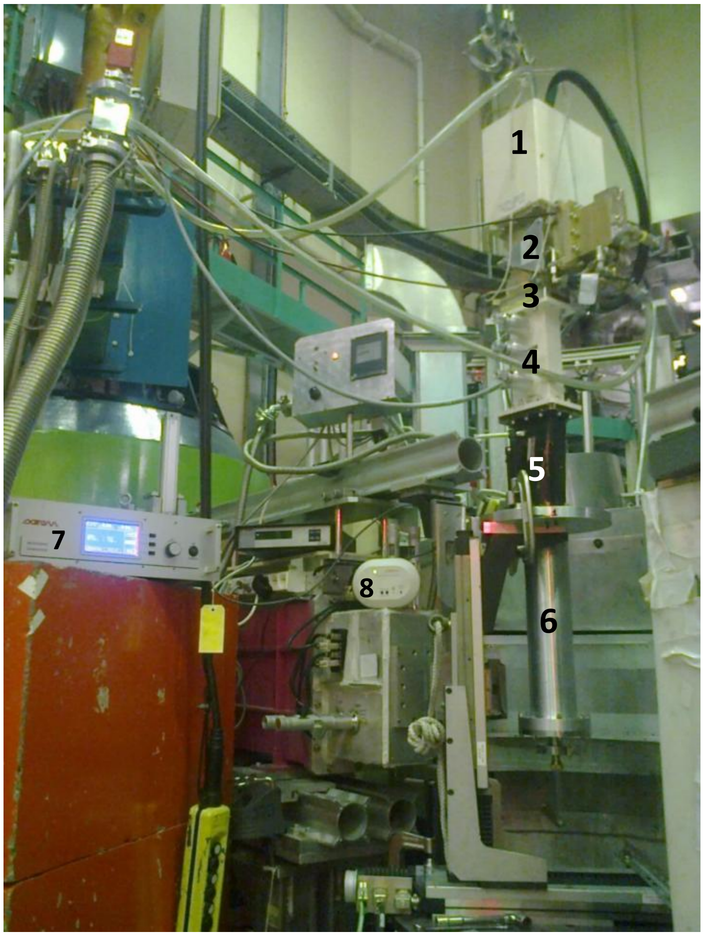

Fig.3. Working MW set-up, mounted on D20: (1) MW generator and magnetron; (2) isolator; (3) quartz window; (4) 3-stub tuner; (5) transition waveguide; (6) applicator; (7) power supply; (8) MW survey meter.

It is possible to easily charge the sample from the bottom of the applicator (Figure 4).

The sample (1 gram pellet, 8mm diameter and about 1 cm thick, embedded in graphite powder - which is a good MW absorber and a catalyst) is placed in the reaction tube – a quartz tube open to the top, thus being exposed directly to the MW radiation, and close to the bottom (Figure 4 and 5) - supported by a small amount of cotton wool; the position of the reactor tube in the applicator can be manually and easily adjusted by the operator. The best MW/sample coupling position is found when the difference between the forward (FP) and the reflected (RP) power is at its highest value – which corresponds to the maximum amount of energy absorbed by the sample, and hence maximum heating achieved at the sample position.

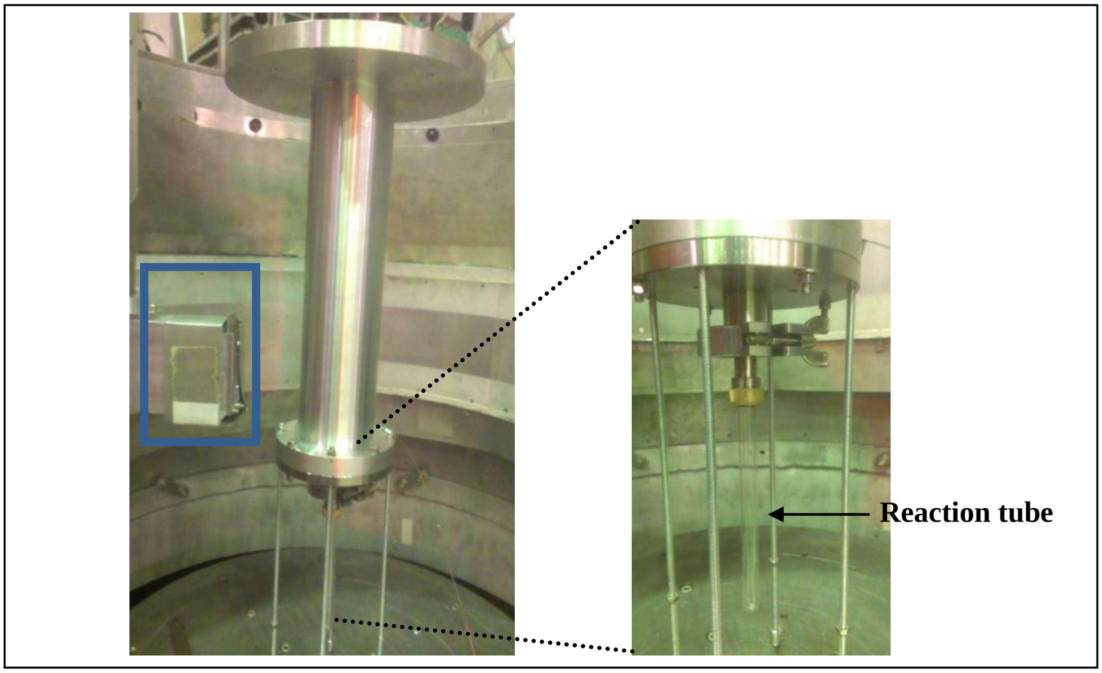

Fig.4. Applicator (with neutron window in blue, on the left) and a zoom of the reaction tube, loaded into the applicator (showed on the right).

After maximizing 1) the power absorbed by the sample, by using the 3-stub tuner until the RP is found at its minimum value and 2) the centering of the sample in the beam, the reaction can start. Step 2 is possible by means of a microcontroller table (Figure 6).

Step 1 and 2 can be optimized by using a dummy sample first (usually, graphite in powder or in pellet), working in off situ mode.

Once all the parameters are satisfactory, it is possible to charge the sample and enable a remote control function on the MW power supply. This has been implemented - and is now easily accessible - in Nomad server; this allows performing the reaction in situ, operating from the beam line workstation.

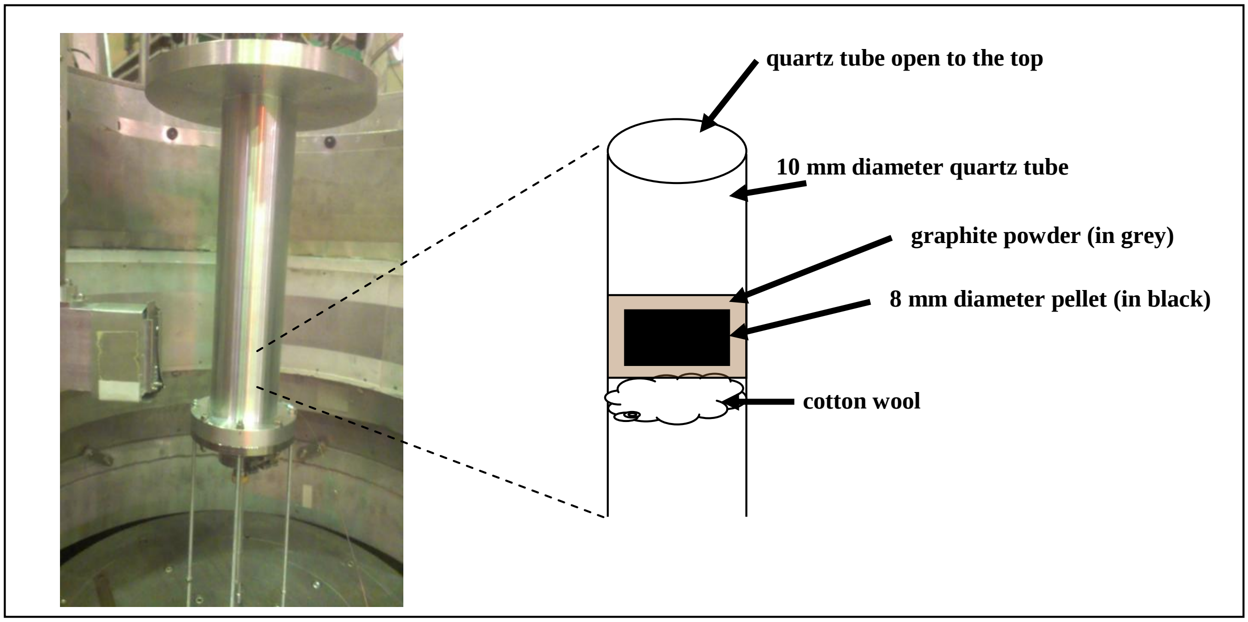

Fig.5: Scheme of the quartz tube+pellet (right), inside the applicator. The pellet is embedded in graphite (powder), which acts as susceptor for the reaction, being a good absorbent of MWs. The cotton wool is needed for supporting the pellet in the quartz tube (but it is inert for both neutrons and sample).

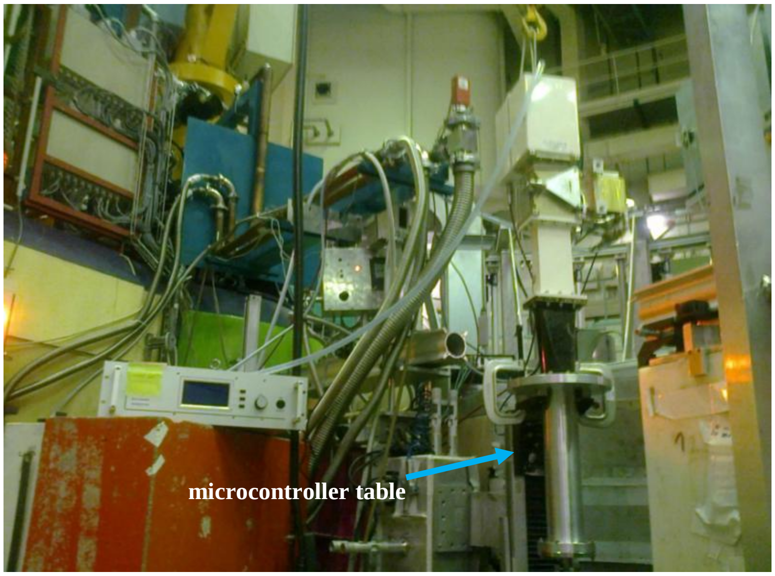

Fig.6. The microcontroller table moves the MW set-up vertically, horizontally and on the detector plane (ω angle), in order to allow the best centering position of the sample in the neutron beam, after the best coupling position MW/sample has been found.

As said above, different geometries for the MW set-up have been tested. Figure 7(a) shows a sequence of: MW generator, isolator, H-bend waveguide, linear iris tuner, linear waveguide (2 bits), E-bend waveguide, transition waveguide, and applicator, which was a configuration showing a very high RP. This was possibly due to the presence of the two bend waveguides (H-type (in green) and E-type (in purple)), which complicated the electromagnetic field, making impossible to heat the sample.

We rearranged the system (Figure 7(b)), taking off the H-bend and linear waveguides bits, thus shortening the MW radiation path. Further, we decided for a different tuning system, changing the linear iris tuner (in red, in Figure 7(a)) with a 3-stub tuner (in red, Figure 7(b)). This second configuration enabled us to lower the RP, however not sufficiently for triggering the reaction.

We finally decided to go for a straight configuration, thus realizing the working geometry (Figure 3).

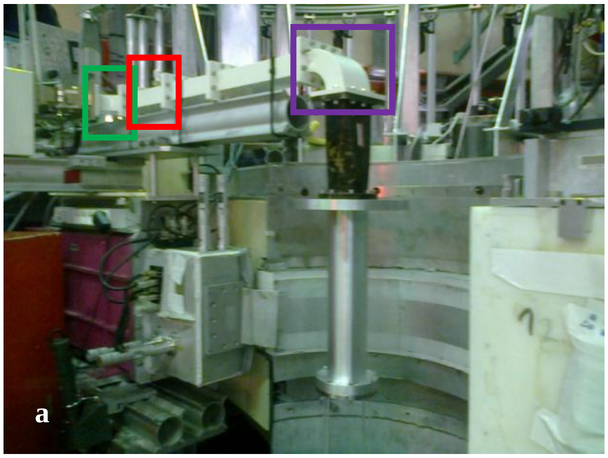

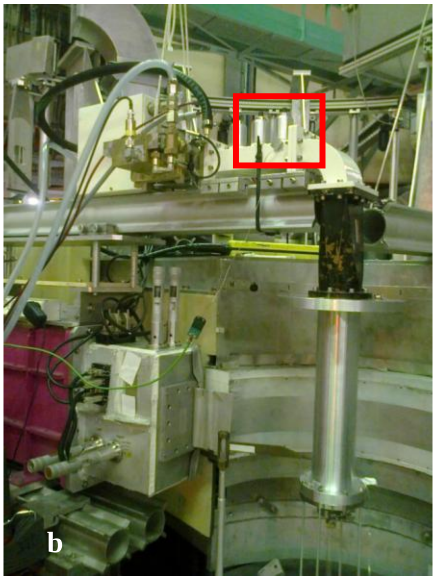

Fig.7(a). MW generator, isolator, H-bend waveguide (in green), linear iris tuner (in red), linear waveguide (2 bits), E-bend waveguide (in purple), transition waveguide, applicator.

Fig.7(b). MW generator, isolator, 3-stub tuner (in red), E-bend waveguide, transition waveguide, applicator.

We successfully achieved the first target of this LTP, by performing, for the first time, the in situ MW-promoted reaction followed by PND of TiC formation, by starting from Ti_{powder}+C_{powder} (embedded in graphite) and results are given in Data 1, which shows 4 patterns:

1) in red, beginning of the reaction (α-Ti+C);

2) in green, co-existence of α and β-Ti phases - β-Ti appears after 30” from the switch on of MWs;

3) in blu, co-existence of β-Ti and TiC phases (while α-Ti is already consumed) - TiC appears 50” after the switch on of MWs;

4) in yellow, only TiC and graphite are present at the end of the reaction (graphite acts as susceptor, therefore is in excess all along the reaction).

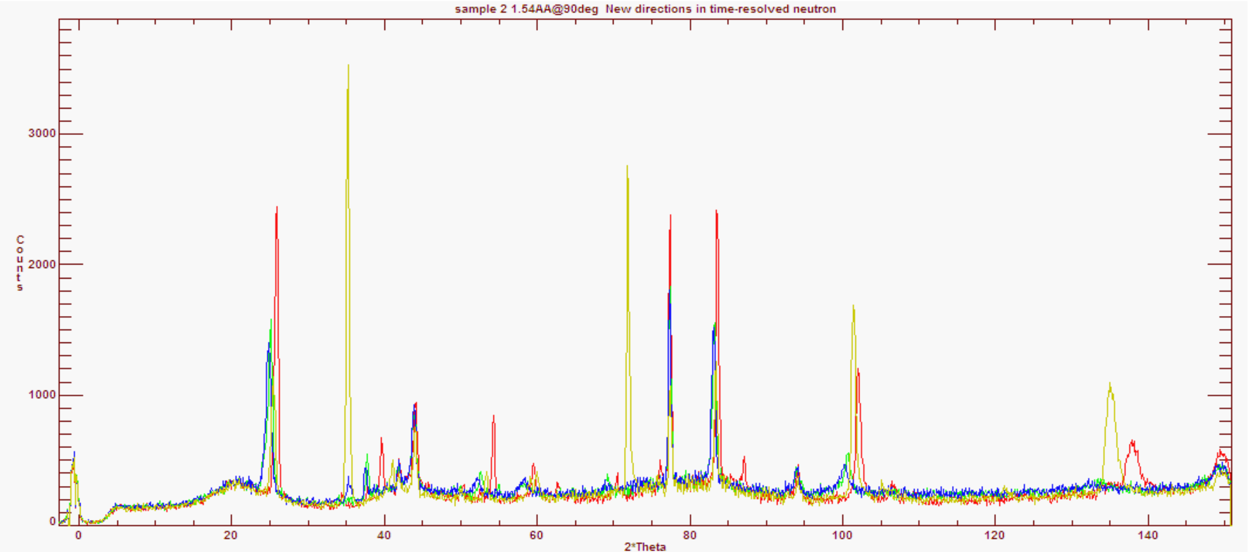

Data 1: Data collected in situ on D20, on 20/02/2013 (500W MW power transferred into the sample; one pattern collected every 10 sec, 90 degrees take off angle, 1.54Å).

Phase two aimed to achieve a precise temperature measurement method for MW reactions. This is not a trivial process as, within the sample, inhomogeneous heating may occur at the millimeter – or sub-millimeter scale. Further, the two "traditional" systems for temperature measurements, thermocouples and pyrometers, are unreliable as the first may cause perturbation of the MW field and the second only gives surface temperature - which will be the coolest part of the sample, due to the nature of inverse temperature profile found in MW heating mechanism [11, 12].

To overcome these difficulties and avoiding misleading temperature measurements, we opted for a crystallographic thermometer, by taking advantage of both the presence of carbon graphite in all our samples and the fact that its linear thermal expansion is known with a good accuracy for a wide range of temperatures – from 293 to 1473K - in literature [13, 14].

From Eq.1, the c-axis value at a given temperature T can be calculated:

$$c(T)=c_{Tr} + \alpha\, c_{Tr}\, (T-Tr) \qquad \text{Eq. 1}$$

where α is the linear thermal expansion ($27.7(\pm 0.6)\times 10^{-6}$ K^{-1}), $c(T)$ and c_{Tr} (=6.7079Å, at 298K) are the c-axis values at the unknown and at the reference temperature respectively; T and Tr are the unknown and the reference temperature, respectively. The unknown temperature T can be then derived from Eq.1:

$$T = T_r + \frac{c(T) - c_{Tr}}{\alpha} \qquad \text{Eq.2}$$

where $c(T)$ is calculated by performing sequential refinement of in situ processes.

The error on T is given by the root mean square deviation (RMSD) method. If $\overline{T} = T - T_r$ and $\overline{c} = c - c_r$, then Eq.2 can be rewritten as:

$$\overline{T} = \frac{\overline{c}}{\alpha} \qquad \text{Eq.3}$$

and the error on $\overline{T}$ is given by:

$$\frac{\delta\overline{T}}{\overline{T}} = \sqrt{\left(\frac{\delta\overline{c}}{\overline{c}}\right)^2 + \left(\frac{\delta\alpha}{\alpha}\right)^2} \qquad \text{Eq.4}$$

Preliminary results show that the $\alpha \rightarrow \beta$ transition for Ti occurs around 780 °C, while TiC starts to form at around 980 °C. The maximum temperature achieved during this reaction has been found at 1122 °C.

In **Phase three** we aimed to optimize the remote control for both 1) power supply and 2) 3-stub tuner. While we achieved point 1, being now possible to switch on and off the reaction directly and easily from Nomad server during measurements, point 2 (automation of the 3-stub tuner) was found to be much more complex and time consuming than expected. For future developments, whilst a manual tuning has been shown sufficient for triggering the reaction, the use of an automatic tuner (commercially available) would represent the best alternative for implementing the actual set-up.

Phase four: Several chemical systems have been processed in our MW set-up (Table 1). Some of them were successfully processed, some others did not give the results we wished to obtain (for example, no peak appearance observed during heating, hence not enough power transferred into the sample). This can be due to different problems (very stable starting materials which require very high activation energy and/or not enough graphite powder used as susceptor and/or not perfect height/position of the reaction tube into the applicator which means not enough MW heating achieved…). Most of these systems have been processed very recently (last reactor cycle: 4th-9th July and 17th-19th July 2013), therefore Data 2-Data 9 report only preliminary results.

Chemical system (1 g pellet - susceptor in all cases)	***√ = peak appearance*** ***X = no reaction***
1) W + C (1:1)	**X**
2) Ta + C (1:1)	**X**
3) WO_2 + C	**X**
4) Ti – W – C (0.8:0.2:1)	**√**

5) Nb_2O_5 + C	√
6) Ta_2O_5 + C	√
7) Ta – Ti – C (1:1:2)	√
8) Ta – W – C (0.7:0.3:2)	X
9) Ti – W – C (1:1:1)	√
10) Ti – W – C (0.1:0.9:1)	√
11) Ti – W – C (0.2:0.8:1)	√
12) Ti – W – C (0.3:0.7:1)	√
13) Ti – W – C (0.3:0.6:1)	√
14) Ti – W – C (0.2:0.8:1)	√
15) Ti – W – C (0.1:0.9:1)	√
16) Ta –Ti – C (0.1:0.9:2)	√
17) Ta –Ti – C (0.2:0.8:2)	√
18) Ta –Ti – C (0.3:0.7:2)	√
19) Ta –Ti – C (0.4:0.6:2)	√
20) Ta –Ti – C (0.5:0.5:2)	√
21) Ta –Ti – C (0.6:0.4:2)	√
22) Ta –Ti – C (0.7:0.3:2)	√
23) Ta –Ti – C (0.8:0.2:2)	√
24) Ta –Ti – C (0.9:0.1:2)	√
25) Ti –WO_2 – C (0.3:0.7:1)	X
26) Ti –WO_2 – C (0.4:0.6:1)	X
27) Ti –WO_2 – C (0.5:0.5:1)	X
28) Ti –WO_2 – C (0.6:0.4:1)	√
29) Ti –WO_2 – C (0.7:0.3:1)	√
30) Ti –WO_2 – C (0.8:0.2:1)	√
31) Ti –WO_2 – C	√

(0.9:0.1:1)	
32) Ti –Ta_2O_5 – C (0.9:0.1:2)	√
33) Ti –Ta_2O_5 – C (0.8:0.2:2)	√
34) Ti –Ta_2O_5 – C (0.7:0.3:2)	X
35) Ti –Ta_2O_5 – C (0.6:0.4:2)	X
36) Ti –TiO_2 – C (0.9:0.1:1)	√
37) Ti –TiO_2 – C (0.8:0.2:1)	√
38) Ti –TiO_2 – C (0.7:0.3:1)	X
39) Ti –TiO_2 – C (0.6:0.4:1)	X
40) Ti – Nb_2O_5 – C (0.9:0.1:1)	X
41) Ti – Nb_2O_5 – C (0.8:0.2:1)	√
42) Ti – Nb_2O_5 – C (0.7:0.3:1)	√
43) Ti – Nb_2O_5 – C (0.6:0.4:1)	√
44) Ti – Nb_2O_5 – C (0.5:0.5:1)	√
45) Ti – Nb_2O_5 – C (0.4:0.3:1)	√

Table 1. All the systems we processed by means of MWs, in situ. Green symbol (√) stands for a response to the MW field, red cross (X) means that no reaction (no peak appearance) occurred.

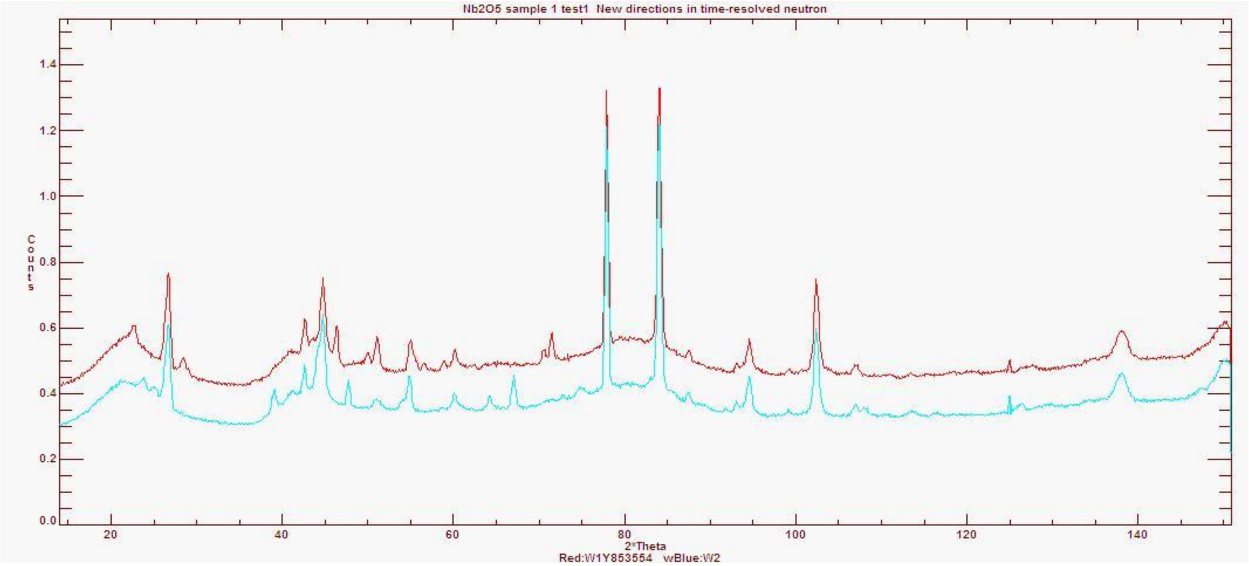

Data 2. Nb_2O_5 + C: in red = before reaction; in light blue = after MW reaction.

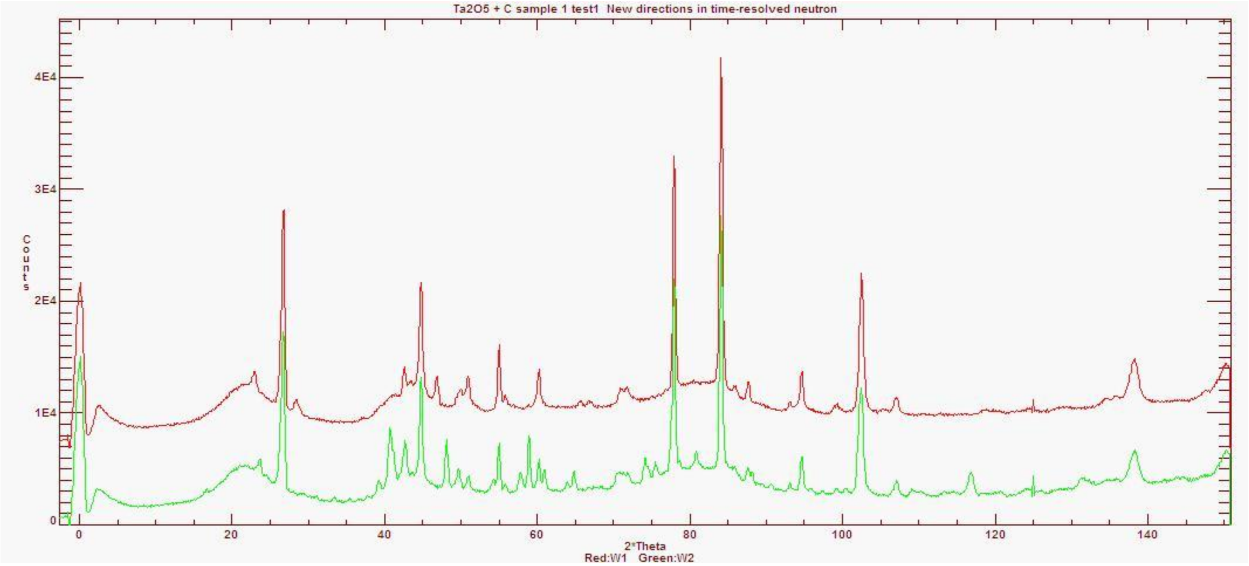

Data 3. Ta_2O_5 + C. In red = before reaction; in green = after reaction.

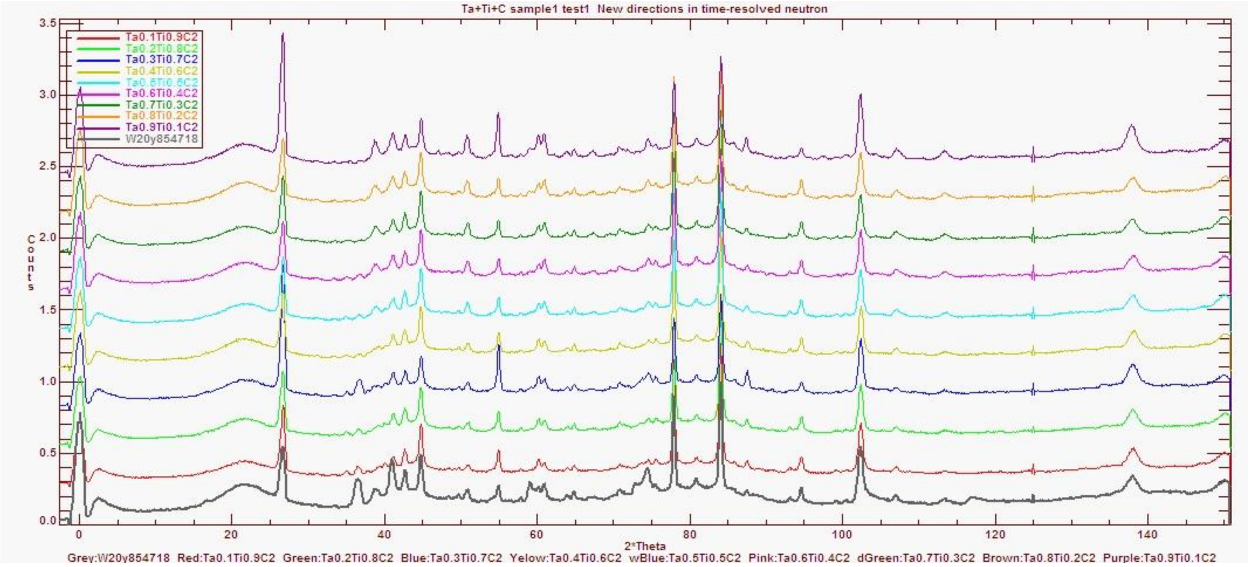

Data 4. $Ta_{(1-x)}Ti_xC_y$ with (x=0.1-0.9 $\Delta x = 0.1$) and (y=2). From the bottom (in red=$Ta_{0.1}Ti_{0.9}C_2$)→ upwards (in violet=$Ta_{0.9}Ti_{0.1}C_2$); in grey = $TaTiC_2$ (1:1:2).

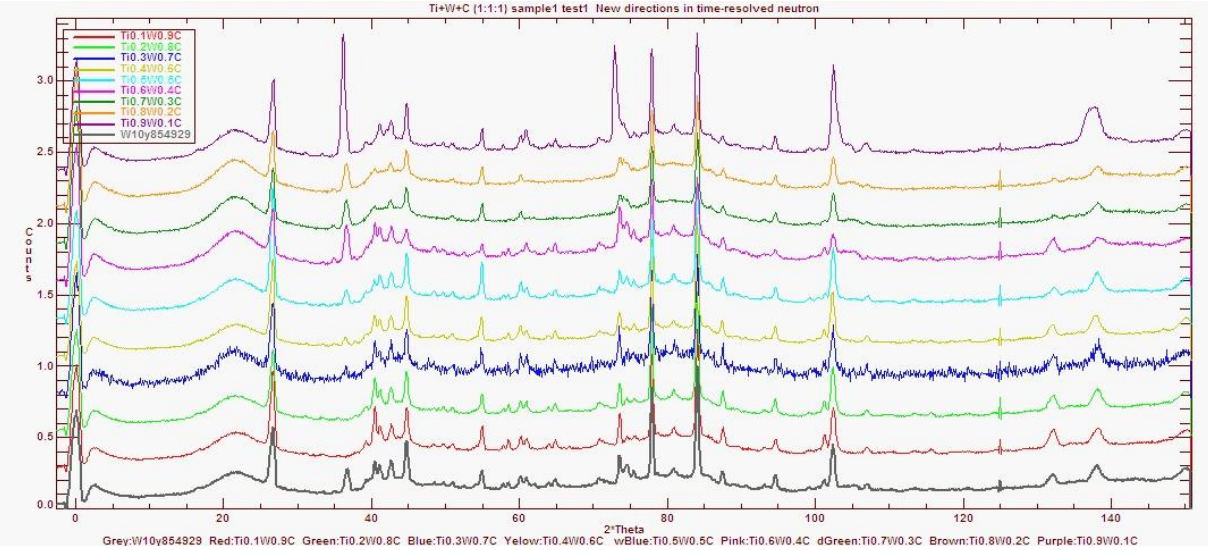

Data 5. $Ti_{(1-x)}W_xC_y$ with ($x=0.1-0.9$ $\Delta x = 0.1$) and ($y=1$). From the bottom (in red=$Ti_{0.1}W_{0.9}C_1$)→ upwards (in violet = $Ti_{0.9}W_{0.1}C_1$); in grey = TiWC (1:1:1).

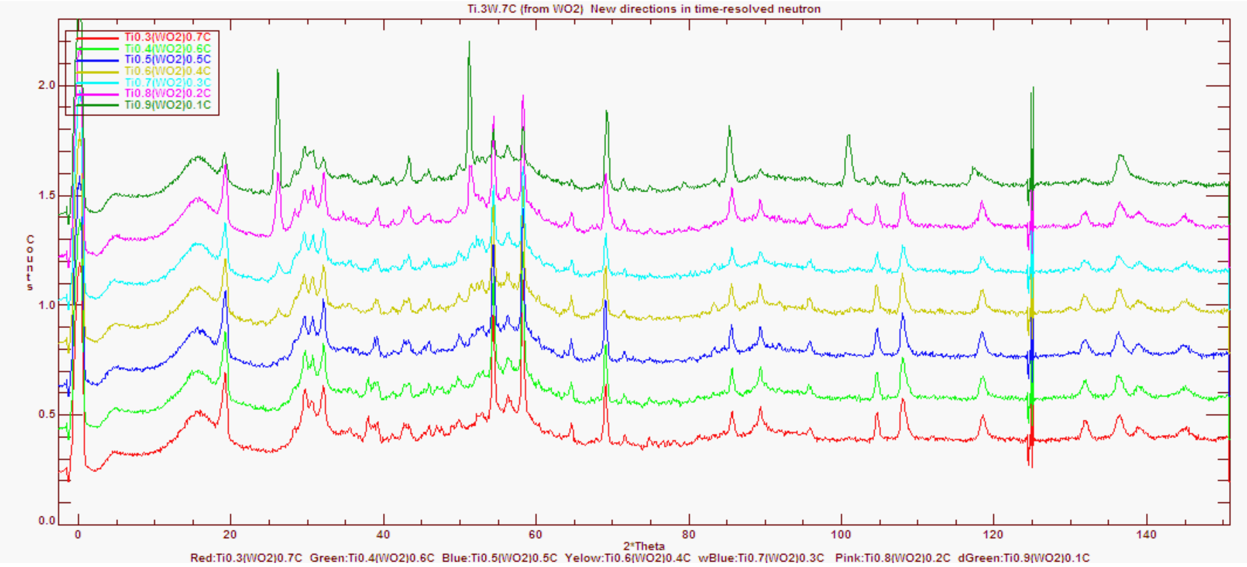

Data 6. $Ti_{(1-x)}(WO_2)_xC_y$ with ($x=0.1-0.7$ $\Delta x = 0.1$) and ($y=1$). From the bottom (in red= $Ti_{0.3}(WO_2)_{0.7}C_1$)→ upwards (dark green = $Ti_{0.9}(WO_2)_{0.1}C_1$).

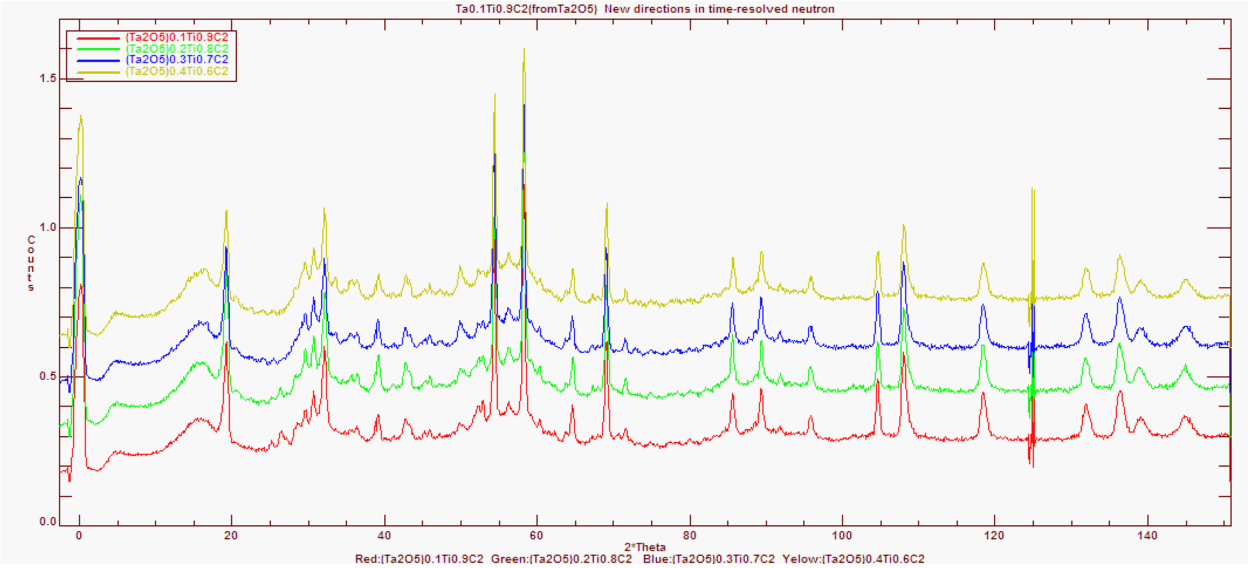

Data 7. $Ti_{(1-x)}(Ta_2O_5)_xC_y$ with (x=0.1-0.4 Δx = 0.1) and (y=2). From the bottom (in red= $Ti_{0.9}(Ta_2O_5)_{0.1}C_2$)→ upwards (yellow = $Ti_{0.6}(Ta_2O_5)_{0.4}C_2$).

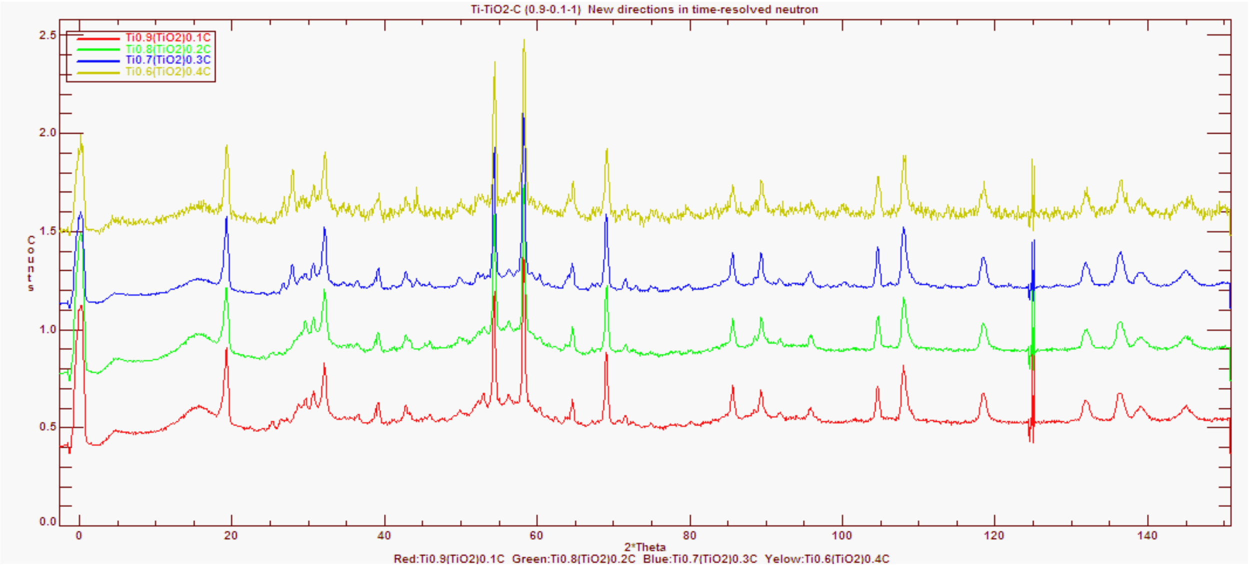

Data 8. $Ti_{(1-x)}(TiO_2)_xC_y$ with (x=0.1-0.4 Δx = 0.1) and (y=1). From the bottom (in red= $Ti_{0.9}(TiO_2)_{0.1}C$)→ upwards (yellow = $Ti_{0.6}(TiO_2)_{0.4}C$).

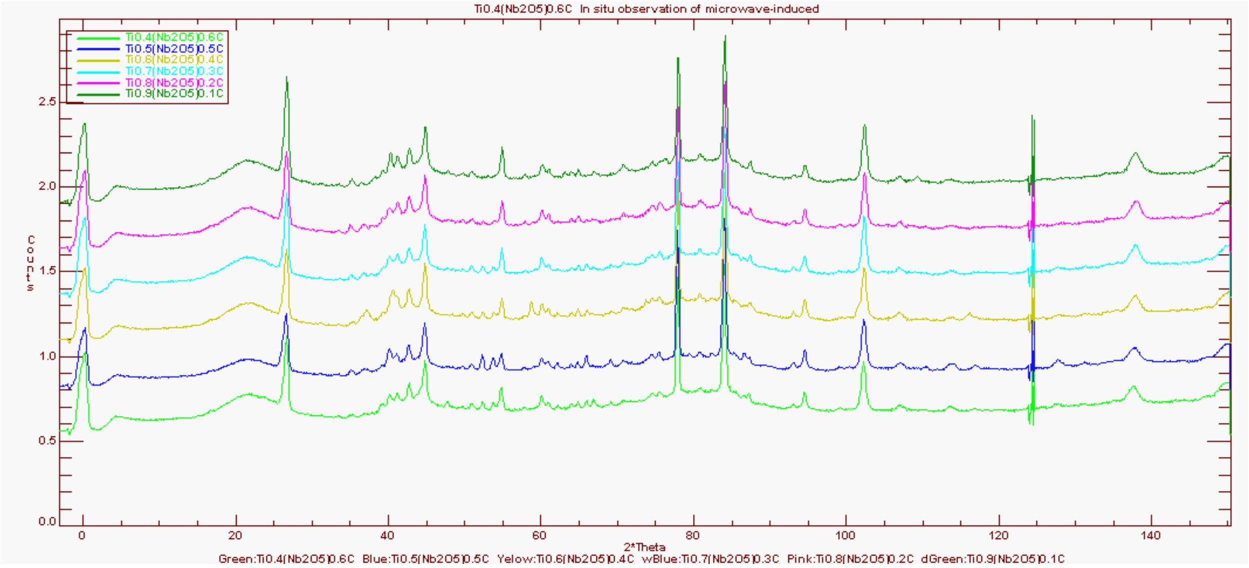

Data 9. $Ti_{(1-x)}(Nb_2O_5)_xC_y$ with (x=0.1-0.6 $\Delta x = 0.1$) and (y=1). From the bottom (in light green= $Ti_{0.4}(Nb_2O_5)_{0.6}C$)→ upwards (dark green = $Ti_{0.9}(Nb_2O_5)_{0.1}C$).

Bibliography

1. Bykov, Y.V. and V.E. Semenov, *High-temperature microwave processing of materials.* Journal of Physics D: Applied Physics, 2001. **34**: p. R55-R75.
2. Cheng, J., et al., *Microwave reactive sintering to fully transparent aluminum oxynitride (ALON) ceramics.* Journal of Materials Science Letters, 2001. **20**: p. 77-79.
3. Fang, Y., et al., *Enhancing densification of zirconia-containing ceramic-matrix composites by microwave processing.* Journal of Material Science, 1997. **32**: p. 4925-4930.
4. Katz, J.D., *Microwave Sintering of Ceramics.* Annual Review of Material Science, 1992. **22**: p. 153-170.
5. Schiffman, R.F., *Commercializing Microwave Systems: Paths to success or Failure.* Ceramic Transactions, 1995. **59**: p. 7-17.
6. Agrawal, D., et al., *Microwave Processing of Ceramics, Composites and Metallic Materials*, in *Microwave Solutions for Ceramic Engineers*, D.E. Clark, et al., Editors, The American Ceramic Society: Westerville, Ohio.
7. Rao, K.J., et al., *Synthesis of Inorganic Solids Using Microwaves.* Chemical Materials, 1999. **11**: p. 882-895.
8. Menéndez, J.A., et al., *Microwave heating processes involving carbon materials.* Fuel Processing Technology, 2010. **91**: p. 1-8.
9. Michael, D., D.M.P. Mingos, and D.R. Baghurst, *Microwaves in Chemical Synthesis*, in *The New Chemistry*. 2000, Cambridge University Press.
10. Vallance, S.R., *Microwave Synthesis and Mechanistic Examination of the Transition Metal Carbides*, in *School of Chemistry*. 2008, University of Nottingham.
11. Wang, J., et al., *Evidence for the Microwave Effect During Hybrid Sintering.* Journal of the American Ceramic Society, 2006. **89**(6): p. 1977-1984.
12. Harrison, A., et al., *In situ neutron diffraction studies of single crystals and powders during microwave irradiation.* Faraday discussions, 2002. **122**: p. 363-379.

13. Winkler, B., et al., *In situ observation in the formation of TiC from the elements by neutron diffraction.* Journal of Alloys and Compounds, 2007. **441**: p. 374-380.
14. Nihira, T. and T. Iwata, *Temperature Dependance of Lattice Vibrations and Analysis of the Specific Heat of Graphite.* Physical Review B, 2003. **68**.